




Extreme compression of planetary gases: High-accuracy pressure-density measurements of hydrogen-helium mixtures above fourfold compression

Sakun Duwal,^{*} Raymond C. Clay III, Marcus D. Knudson, Jeremiah Boerner , Kyle Cochran , Joshua Usher, Daniel Dolan, Bernardo Farfan, Chris de La Cruz, Jacob Banasek, and Christopher T. Seagle
Sandia National Laboratories, Albuquerque, New Mexico 87125, USA

Richard Hacking and Sheri Payne

National Security Technologies, Albuquerque Operations, Albuquerque, New Mexico 87125, USA

Charlie Zoller , Muhtar Ahart, and Russell J. Hemley
University of Illinois Chicago, Chicago, Illinois 60607, USA



(Received 13 July 2023; revised 7 February 2024; accepted 13 February 2024; published 4 March 2024)

Hydrogen (H_2) and helium (He), the most abundant elements in the universe, pose a unique challenge in measuring the equation of state of the mixture, owing to their differing physical properties. There remains a need for data with high enough precision to discriminate between existing equation of state (EOS) mix models in order to understand the internal structure of gas-giant planets. Here, we have measured the EOS of precompressed H_2 -He mixtures at conditions directly relevant to the planetary interiors using hypervelocity gas guns and Sandia's Z machine with less than 10% uncertainty in density, enabling validation of mixture models. We precompressed 50:50 molar mixtures of H_2 -He to 0.1–0.2 GPa and directly measured particle velocity (in gas-gun experiments) and shock velocities (in Z-machine experiments). To complement the experimental efforts, we also computed the Hugoniot of precompressed H_2 -He mixtures using density-functional-theory-based molecular dynamics. We observe approximately 3- to 4.3-fold density compression at pressures up to 44 GPa.

DOI: [10.1103/PhysRevB.109.104102](https://doi.org/10.1103/PhysRevB.109.104102)

I. INTRODUCTION

Hydrogen (H_2) and helium (He), the main components of the gas-giant planets, are the simplest electronic systems, yet both exhibit far more complex behavior, such as phase transitions, ionization, and nonideal mixing, which creates challenges at high pressure to determine the equation of state (EOS) of these mixtures. Our knowledge of the EOS of H_2 -He at different pressure-temperature regimes is pivotal to understanding the origin and evolution of these gas-giant planetary systems. Attempting to map out the phase diagram of H_2 -He mixtures has been an ongoing challenge on both the experimental and theoretical fronts. Several key phenomena, such as molecular decomposition of H_2 to H^+ and ionization, occur under dynamic conditions, which makes modeling this system significantly more challenging [1,2].

To date, several theoretical studies [3–9] have attempted to model various gas-giant planets; however, the results from these studies vary significantly, often with conflicting results. This disparity highlights the pressing need for reliable experimental data to benchmark the theoretical approximations. Even though a few studies have investigated precompressed pure H_2 (or deuterium) [10–14] and pure He [15–19] in dynamic conditions, few advancements [20–22] have been made in the field of H_2 -He mixtures due to the complexities

involved in those experiments, especially due to the challenge associated in confining the fluid mixtures when they cannot be cryogenically mixed. While one can cryogenically load H_2 and He separately, it is impossible to homogeneously mix H_2 -He cryogenically due to the incompatible liquid stability range: H_2 only exists in a liquid form between 20 and 14 K [23], while He exists as a liquid between 4 and 0.9 K [24]. Therefore, precompression of a gaseous mixture of H_2 -He is the only method to achieve high-density states of homogeneous fluid mixtures of H_2 -He, which exist as a homogeneous supercritical fluid mixture below 5 GPa [25,26].

Plate impact techniques at Sandia National Laboratories' (SNL's) Z machine and gas gun provide the potential to obtain higher-precision EOS measurements of precompressed H_2 -He mixtures than can be obtained from laser-shock studies because of larger sample sizes, longer shock duration, and shock steadiness. Combining the high-fidelity output provided by these plate impact studies with the measures taken to characterize initial density and refractive index, we provide EOS measurements of the fluid mixtures with less than 10% uncertainty in density. This high-precision EOS information can be used to distinguish and benchmark various planetary models.

Another challenge, and key factor, that is presented with H_2 -He mixtures is the absence of initial density or refractive index measurements, which are very sensitive in density-compression analysis and can have dramatic effects on the final Hugoniot determination. As such, since the previous

^{*}sduwal@sandia.gov

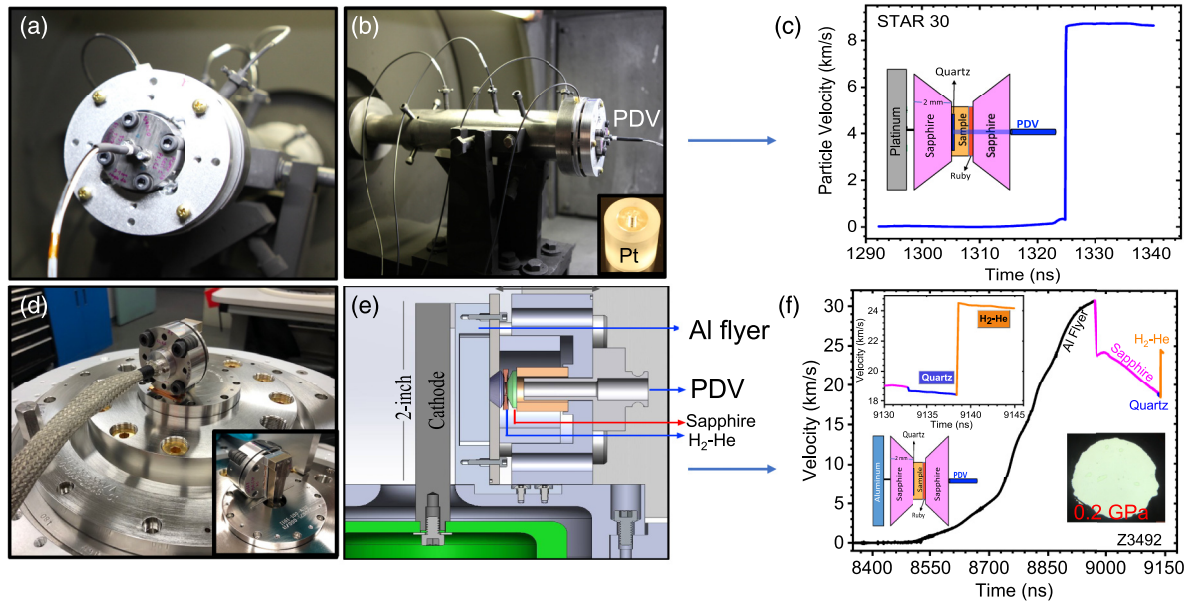


FIG. 1. (a),(b) Experimental configuration showing the precompression cell in a two-stage-light-gas-gun experiment at the STAR facility [inset in (b): Pt projectile]. (c) Representative experimental PDV velocity trace from STAR gas-gun experiments. Particle velocities were measured using an aluminum spot coating at the quartz/sample interface. (d) Experimental configuration in a stripline geometry Z experiment (inset: backside of stripline geometry). (e) Cross section of the schematic of a precompression cell (approximately 50 mm wide and 20 mm tall). (f) Representative experimental velocity trace with true velocities from a Z experiment. Black line: aluminum flyer velocity; magenta line: sapphire shock velocity through a 3.5-mm-thick anvil; blue line: quartz shock velocity; orange line: shock velocity from H₂-He sample. Insets: Enlarged view of the shock velocities in the quartz standard and the sample (top left); schematic of the experimental setup (bottom left; not to scale); microphotograph of the loaded H₂-He fluid (3 mm in diameter) at 0.2 GPa taken through the sapphire anvil (bottom right).

study [22] relied on mixing laws for density estimates, and Lorenz-Lorentz equation for refractive index estimates, the absence of constraint and small sample size, coupled with a short experimental duration, have resulted in large systematic uncertainties inhibiting the ability to distinguish between EOS models. In fact, in highly compressible systems such as H₂-He, a 2–3% change in the initial density could lead to a 7–8% change in the final densities.

In the present study, we have shock compressed mixtures of a 50:50 mole% H₂-He (equivalent to 33% atomic He in H-He) in a precompression cell using Sandia’s Z machine and a two-stage-light-gas gun at the Shock and Thermodynamic Applied Research (STAR) Facility. The propagation of the shock wave was monitored using photonic doppler velocimetry (PDV). In the gas-gun studies, the particle velocities were directly measured from the sample, whereas shock velocities from reflecting shock fronts were measured in the Z experiments. To complement the experimental studies, we have also performed *ab initio* calculations. The results show that the experimental and theoretical data are in good agreement with each other.

II. SHOCK COMPRESSION EXPERIMENTS: GAS-GUN AND Z EXPERIMENTS

Mixtures of H₂-He were initially precompressed to 0.1–0.2 GPa inside a precompression cell (Fig. 1) using a high-pressure gas loader and shock loaded using the Sandia Z machine and two-stage-light-gas gun. Figures 1(a) and 1(b) show the experimental setup for gas-gun experiments, and

Fig. 1(c) shows the measured representative particle velocity profile at the quartz/sample interface [Fig. 1(c), inset]. We used Pt flyers as impactors for gas-gun experiments. The primary diagnostic fielded in these experiments was PDV. For the gas-gun experiments, since the shocked sample was transparent, we directly measured the particle velocity from the quartz/sample at an aluminum spot coated to 100 nm on the quartz. The measured shock transit time in the sample was used to determine the shock velocity in the sample. Figure 1(c) plots the measured particle velocity from the quartz/sample interface for a representative gas-gun experiment. The ramplike feature prior to the shock arrival (at 1325 ns) is due to the noise in the fast-fourier transform signal. We note that two-dimensional (2D) cylindrically symmetric Eulerian simulations were performed with the experimental configuration described here (see Supplemental Material [27] and Refs. [28,29]) to ensure the absence of 2D effects during the timescale of the experiment, i.e., the measurements were obtained under uniaxial compression.

Figures 1(d) and 1(e) show the experimental setup for Z experiments. At shock pressures above 35 GPa, the H₂-He mixture becomes reflective (at these pressures the sapphire and quartz shock fronts were also observed to be reflective). Thus, in the Z experiments, the shock velocities were directly measured by PDV. Figure 1(f) plots the measured shock velocity trace from a representative Z experiment, in this case with a peak flyer velocity of 31 km/s. All the raw PDV traces from each experiment are provided in the Supplemental Material [27]. The actual shock velocities shown in Table I were obtained from the measured apparent shock velocities

TABLE I. Experimentally determined Hugoniot states of H₂-He from gas-gun and Z experiments. The flyer velocity (V_F) and shock velocity (U_P) are directly measured in the gas-gun experiments. The flyer velocity (V_F) and shock velocity (U_S) are directly measured in the Z experiments. The initial temperature of the precompressed samples is 298 K. The error in the initial pressure P_0 is less than 2%. The uncertainty in the initial density is in the last digit(s). Particle velocity (U_P) and pressure (P) are determined using the quartz release model [31,32] and errors were calculated using the Monte Carlo method by propagating errors from uncertainties in the observed velocities.

Shot ID	P_0 (GPa)	Thickness (μm)	ρ_0 (g/cm ³)	Transit time (ns)	V_{flyer} (km/s)	Quartz U_s (km/s)	U_P (km/s)	U_S (km/s)	P (GPa)	Compression ρ/ρ_0
STAR24 ^a	0.160	399.5±2.2	0.102(5)	46.5 ± 2.0	4.25±0.05	–	5.76±0.05	8.59±0.37	5.21±0.3	3.03±0.28
STAR20 ^a	0.134	381.0±2.3	0.091(4)	37.0 ± 1.0	5.01±0.04	–	7.02±0.03	10.29±0.29	6.71±0.3	3.15±0.19
STAR38 ^a	0.130	355.7±3.3	0.089(4)	31.0 ± 0.09	5.07±0.05	–	7.86±0.06	11.47±0.11	8.16±0.4	3.18±0.08
STAR30 ^a	0.150	208.8±2.5	0.098(5)	16.80 ± 0.4	5.78±0.05	–	8.78±0.12	12.43±0.33	10.83±0.7	3.41±0.24
STAR39 ^a	0.140	178.0±2.1	0.094(4)	13.7 ± 0.50	5.71±0.05	–	9.57±0.13	12.99±0.50	11.83±0.7	3.80±0.43
STAR40 ^a	0.110	278.0±2.4	0.079(4)	20.0 ± 0.13	6.49±0.05	–	9.79±0.09	13.90±0.15	10.86±0.6	3.38±0.11
STAR31 ^a	0.150	254.1±2.3	0.098(4)	15.33 ± 0.08	6.23±0.06	–	11.99±0.09	16.56±0.17	19.61±0.8	3.62±0.12
Z3546S ^b	0.240	364.9±2.4	0.131(5)	22.33 ± 0.02	18.01±0.06	13.97±0.16	12.69±0.08	16.64±0.07	27.42±3.0	4.21±0.10
Z3546N ^b	0.220	325.8±2.1	0.124(5)	19.22 ± 0.03	16.78±0.07	14.02±0.14	12.73±0.07	16.79±0.07	29.03±4.3	4.13±0.09
Z3668S ^b	0.110	391.7±2.3	0.079(4)	16.00 ± 0.03	22.50±0.06	18.24±0.12	18.95±0.16	24.46±0.24	35.38±4.4	4.43±0.19
Z3492 ^b	0.150	200.9±2.2	0.098(5)	8.10 ± 0.02	30.82±0.05	18.72±0.13	18.44±0.13	24.40±0.14	44.81±5.2	4.30±0.24

^aFor the STAR gas-gun shots, U_P was measured at the window/sample interface, and U_S was obtained from the shock transit time.

^bFor Z shots, reflective shock fronts were recorded from front sapphire, quartz, and sample.

by dividing apparent shock velocities by the indices of refraction for the quartz and sample. The equations used to obtain the refractive indices (n) of precompressed quartz (n_{Q0}) [19] and H₂-He (n_{H_2-He}) [30] were $n_{Q0} = 1.54684 + 0.1461(\rho_0 - 2.649)$ and $n_{H_2-He} = 1 + 0.6\rho$, respectively. The impedance matching method, utilizing the well-established quartz release model by Knudson *et al.* [31,32], was used to determine the shock states, taking the correction of precompressed density and refractive index into account [19].

Eleven experiments were performed on precompressed H₂-He fluid mixtures using the two-stage gas gun (seven experiments) and the Z machine (four experiments). All the pertinent experimental parameters and the resulting Hugoniot data are summarized in Table I, and the raw velocity traces are also presented in the Supplemental Material [27] (Figs. S1–S3). The Rankine-Hugoniot conservation equations were used to calculate the postshock conditions. Here ρ , P , U_S , and U_P are the density, pressure, shock velocity, and particle velocity, respectively, and the subscript 0 denotes the initial states,

$$P = P_0 + \rho_0 U_S U_P, \quad (1)$$

$$\rho = \frac{\rho_0 U_S}{U_S - U_P}. \quad (2)$$

III. CONSTRAINING THE EOS MODELS: ISOTHERMS OF HYDROGEN, HELIUM, AND HYDROGEN-HELIUM

To calculate the final Hugoniot states, the initial precompressed density needs to be precisely determined. We have measured the sound velocities of H₂-He using Brillouin spectroscopy in a diamond anvil cell to determine the initial density and refractive index. The densities are summarized in Fig. 2. In addition to the experimental work, we have further benchmarked the densities of H₂-He by first computing the densities of the end members, H₂ and He, using theoretical calculations. Upon excellent agreement of these calculated end-member densities with the experimentally reported values, we employed the same method to the H₂-He mixture,

which shows an excellent agreement with the experimental data using Brillouin measurements. We have measured the sound velocities of H₂-He fluid mixtures, which is directly related to the density of the fluid through Eq. (3) [33], where ρ is the final density, ρ_0 is a reference density, $\gamma = Cp/Cv$, and U_l is the longitudinal sound velocity of the material,

$$\rho - \rho_0 = \int_{P_0}^P dP \gamma / U_l^2. \quad (3)$$

As all the details require a much deeper discussion, the sound velocity and density measurements from the Brillouin

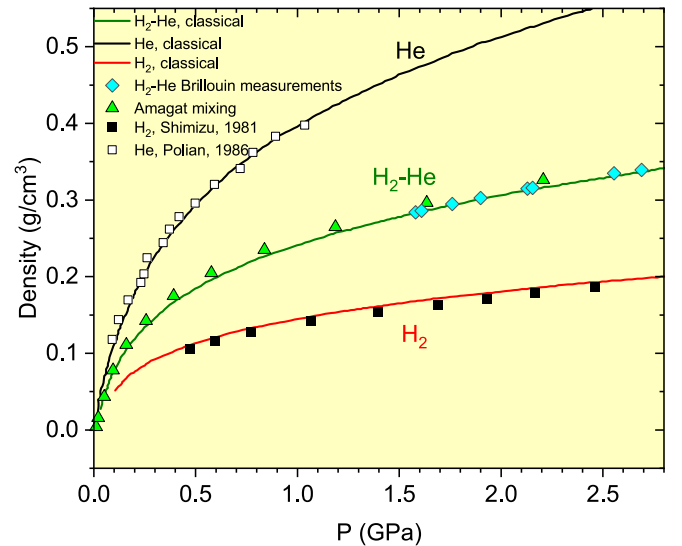


FIG. 2. Isotherms of H₂-He fluid mixtures. Solid lines represent the theoretical calculations; green triangles represent isotherms computed using the Amagat mixing law. Cyan diamond symbols are the experimentally measured densities using Brillouin measurements. Open and filled squares are experimentally obtained densities for H₂ [34] and He [35], respectively.

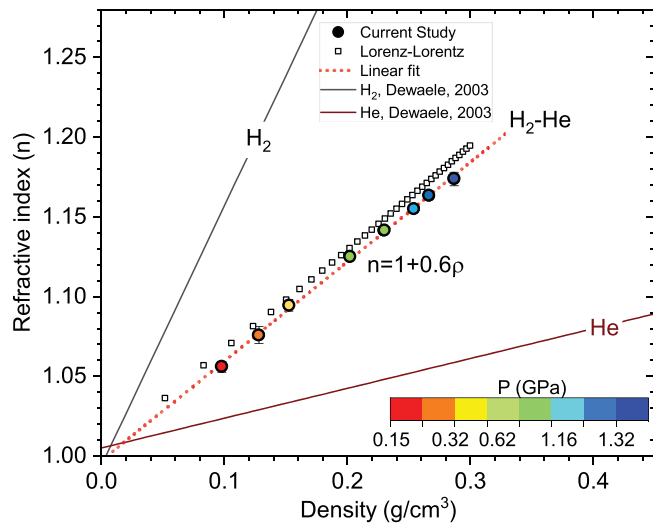


FIG. 3. Experimentally measured refractive indices of H₂-He (circles) compared with the calculated refractive indices using the Lorenz-Lorentz relationship (open squares). The colors represent the pressure for a given density. The refractive indices of the end members [36] are also shown for comparison.

measurements are published in greater detail in a separate paper [30]. Using the measured sound velocities at 532 nm, we have also determined the refractive index of the H₂-He mixture (details published in [30]). The refractive index is related to the sound velocity by the following relation:

$$n = U_l / [\sin(\theta_{sc}/2) * U_l(bs)], \quad (4)$$

where θ_{sc} corresponds to the scattering angle, and $U_l(bs)$ corresponds to the backscattered velocity at $\theta = 180^\circ$.

Figure 3 shows the experimentally measured refractive indices as a function of density. We have also compared the experimentally determined refractive indices with the refractive indices calculated using the Lorenz-Lorentz relationship. The Lorenz-Lorentz calculations are in good agreement with the experimental data at $P > 0.2$ GPa. However, at 0.15 GPa (most of our initial precompression pressure), the experimentally observed value is slightly smaller. As there are no absorption lines on both H₂ and He at 532 or 1550 nm, we do not expect a strong change in the refractive index between these two wavelengths. Therefore, no wavelength correction to the refractive index was applied for the PDV data. When a material's refractive index is linear in density, as shown in Fig. 3, the window correction is the intercept of the linear fit, which is 1 for H₂-He. For our final Hugoniot analysis, we have used the carefully measured true densities and refractive indices of the H₂-He fluid mixtures using Brillouin study in order to obtain highly accurate EOSs of the fluid mixture.

To complement the experimental results, we constructed two EOSs based on differing levels of theory. For the first, we used first-principles molecular dynamics (FPMD) with a potential energy surface for the 50-50 H₂-He mixture determined using density functional theory molecular dynamics (DFT-MD) [37,38]. For the second, we used an EOS for pure H₂ and for pure He to generate an ideal mix EOS according to the

Amagat-Leduc law [39], henceforth referred to as ‘‘Amagat’s Law.’’ The pure state EOSs were also generated using FPMD. The calculated isotherm results are summarized in Fig. S4 in the Supplemental Material [27].

All calculations were done with VASP 5.4.4 [40,41]. We used the number of particles, volume, temperature (NVT) ensemble with an Anderson thermostat (thermostat frequency every 20 steps) with a time step of $t = 0.2$ fs for all points. We used cubic simulation cells with 64 He atoms and 128 H atoms, thus preserving a 50-50 mix of He to H₂. For the electronic structure, we used the Mermin free-energy functional [42] based on the ground-state Perdew-Burke-Ernzerhof (PBE) [43] functional, a plane-wave cutoff of 1200 eV, and the Baldereschi mean value point. The DFT results are summarized in Tables S1 and S2 in the Supplemental Material [27].

IV. DYNAMIC RESULTS AND DISCUSSION

Figure 4 plots the shock velocity-particle velocity ($U_s - U_p$) relation of H₂-He mixtures obtained from the gas-gun and the Z experiments. The error bars are 1-sigma. A window correction of 1.0 was applied based on the refractive index and density measurements of the fluid mixture for the gas-gun data. For the Z experiments, since the PDV measurements came directly from the reflective shock front, the refractive-index correction for the sample used the refractive index determined from Brillouin measurements in diamond anvil experiments. We chose to fit the obtained $U_s - U_p$ data using a linear relationship. Note that dissociation likely is occurring above U_p of 11 km/s; therefore, the linear fit only suggests as a trend line to the data. We observe a curvature in the $U_s - U_p$ vs U_p data [Fig. 4(b)] at the region where dissociation is expected. Interestingly, our results suggest that the H₂-He Hugoniot behavior is close to that of precompressed hydrogen Hugoniot (dashed black line) obtained from SESAME 5351.

Figure 4(c) shows the pressure vs density compression of H₂-He. Also shown in Fig. 4(c) are Hugoniots of H₂-He computed using PBE (solid lines) and the precompressed Hugoniots of the end members, H₂ and He. Experimentally, we observe 3- to 4.3-fold density compression in H₂-He mixtures. Our experimental data are well within the bounds of the PBE-computed DFT Hugoniots and also falls between the precompressed 0.15 GPa Hugoniots of H₂ and He. PBE and Amagat mixing (square symbols) are in good agreement for 0.11 and 0.15 GPa, suggesting an ideal mixture-like behavior at low pressures. We observe a notable discrepancy (higher at increasing precompression pressure) between the Amagat- and PBE-computed Hugoniots. All Amagat Hugoniots are systematically softer than the DFT H₂-He simulations. We have further investigated the nonideal contribution by comparing the Amagat ideal mix EOS against the full DFT-MD calculations of the mixture; see the Supplemental Material (Fig. S5) [27]. In this study, we attribute the discrepancy between Amagat and DFT to be nonideal contributions. We observe a 20–30% drop in specific volumes and 15–20% drop in the excess energies at a small pressure regime of 10–20 GPa, which is due to the nonideality contribution; see the Supplemental Material (Fig. S7) [27]. It is possible that dissociation or a metallic transition could be playing a role

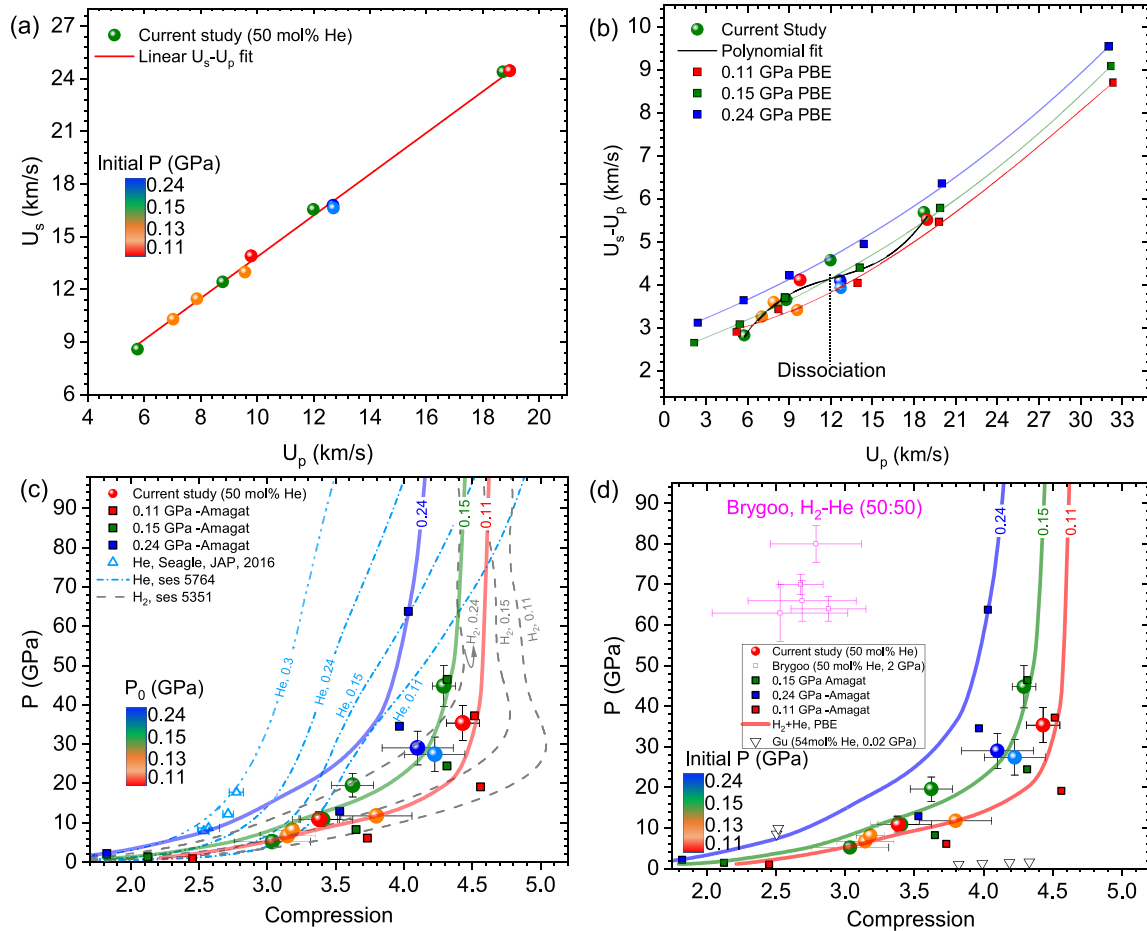


FIG. 4. Hugoniot of H₂-He mixtures. Spheres are the data from the current study. The colors of the sphere symbols represent the initial pressure. (a) $U_s - U_p$ Hugoniot for H₂-He mixtures. The errors lie within the data symbols. The solid red line is the linear fit to the experimental data. (b) Data in $U_s - U_p$ vs U_p space showing a curvature at the dissociation regime. Square symbols are results from DFT-PBE calculations. (c) Pressure-density compression Hugoniot for H₂-He mixtures compared with pure H₂ and He. The solid lines are interpolations for PBE, FPMD results at 0.11, 0.15, and 0.24 GPa initial compression; blue dashed and gray dashed lines are precompressed He Hugoniot from SESAME 5764, and 5351, respectively. (d) Pressure-density compression compared with the literature data [20,22]. Filled square symbols are results from Amagat ideal mixing at different initial pressures; open squares are result from Ref. [22]; black triangles are results from Ref. [20].

and, therefore, could be the reason for this deviation. The dissociation has not been accounted for in the Amagat-Leduc mixing calculations.

In one of the Z experiments, Z3492, we also performed a simultaneous temperature measurement using Streaked Visible Spectroscopy (SVS) system. The time- and wavelength-calibrated streak camera image is shown in Fig. 5(a). The calibration procedure has been discussed in detail in Ref. [44] and is also described in the Supplemental Material [27]. The data show a significant increase in emission as the shock transits from the sapphire window to the quartz window (at 3219 ns). The line-out [Fig. 5(b)] shows a slight dip in emission as the shock transits from the quartz window to the H₂-He sample. Finally, a significant drop in emission is observed, as the shock transits from the sample to the rear sapphire window. The thermal emission data correlates well with the transit times in the quartz and the sample obtained from the velocimetry data. Note that the slope observed in the baseline of the radiance data is caused by decaying shocks. However, as quartz and the sample are expected to be completely opaque

and reflecting at this state, we do not expect any contamination in the data from the light behind the quartz. If the sample is not fully opaque, there would be a possibility that light from other impact surfaces, such as the flyer/sapphire, could contribute to the emission measurements.

We have reduced the obtained spectral thermal emission data to calculate spectral emissivity and then temperature (see the Supplemental Material [27]). The inferred quartz temperature is $28\,700 (\pm 2300)$ K and the temperature at the sample is $24\,600 \pm 1700$ K. The temperature at quartz is consistent (within uncertainty) with the quartz temperature reported by Celliers *et al.* [17] at a shock velocity of 18.45 km/s ($26\,700 \pm 5100$ K). Alternatively, using the quartz as a standard for the intensity calibration, the temperature in the sample comes out to be $(25\,800 \pm 4800)$. Note that the errors reported here only correspond to statistical (random) error, not instrumental (systematic) error. While there are uncertainties in the emissivity obtained in this study, the overall trend seems to be typical of that of a poor metal. Figure 5(c) plots the (Pressure, Temperature) P-T obtained from the experiment, the PBE calculations

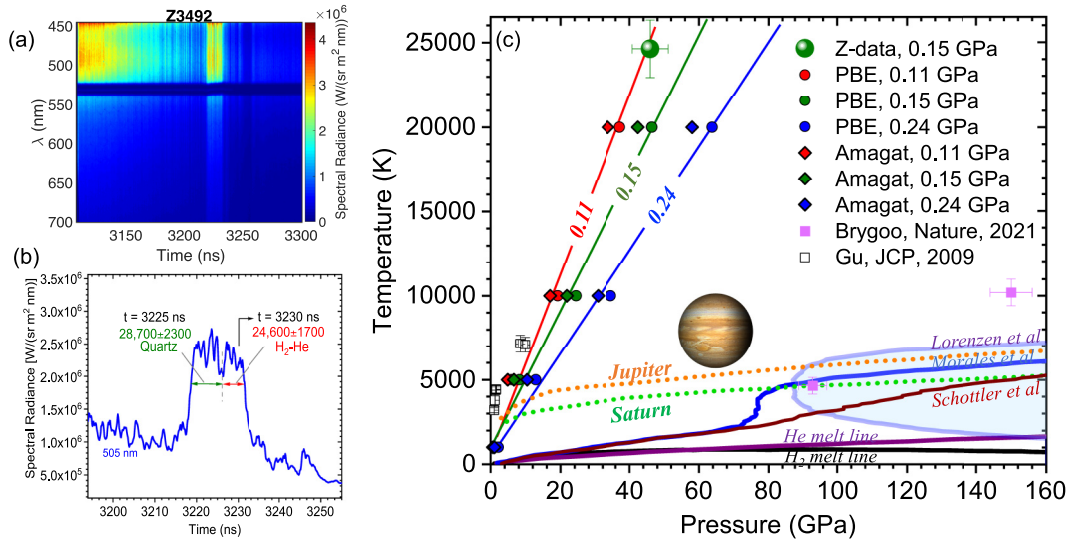


FIG. 5. (a) Streak camera image from the Streaked Visible Spectroscopy system. (b) Line-out from the streak image at 505 nm. (c) Pressure-temperature Hugoniot for H_2 -He mixtures. Sphere symbol is the data from the Z experiment, Z3492 (0.15 GPa); stars, hexagon, and pentagon symbols are PBE-calculated Hugoniot for 0.11, 0.15, and 0.24 GPa precompression, respectively (lines are drawn as a guide for the eye); magenta squares are selected H-He (11 mol% He) laser-shock data from Brygoo *et al.* [22] precompressed to 4 GPa and open squares are data from Gu *et al.* [20] precompressed to 20 MPa.

(circle symbols), and the Amagat mixing (diamond symbols) at different initial pressures of 0.11, 0.15, and 0.24 GPa. The experimentally inferred temperature is 20% higher than the PBE-calculated temperature for 0.15 GPa (24 000 K) PBE Hugoniot. At lower pressures, PBE and Amagat are in good agreement with each other, whereas at higher pressures, there is a slight disagreement, which is likely associated with the nonideal effects.

Despite the overall good agreement between our DFT-MD calculations and experiment for the precompressed Hugoniot for both $U_s - U_p$ and $P - \rho$, experimental temperature measurement indicates that the predicted temperatures along the Hugoniot are noticeably lower than experiment. This is not entirely unexpected and has precedent in the literature. In Ref. [13], it was found that despite very good agreement in the predicted pressure and compression along the principal deuterium Hugoniot, the predicted temperatures varied by up to 1000 K based on the choice of functional. This is attributed to variations in the bond description with the DFT functional. In particular, the specific heat of hydrogenic systems is very sensitive to the strength of the hydrogen bond and how dissociation occurs. Given that the one SVS point is well above the dissociation limit, we expect that the observed temperature of Hugoniot points predicted in DFT is likewise highly sensitive to the choice of exchange-correlation functional. Before concluding that there is a discrepancy between theory and experiment, a more thorough investigation of the functional sensitivities needs to be done.

Our reported Hugoniot data are more compressible than those reported from Brygoo's laser-shock studies [22]. This is expected because the initial precompression pressure is much higher (2–4 GPa) for the laser-shock study compared to the current study (0.1 to 0.2 GPa). In addition, the larger sample size used in these experiments provides a much more

reliable, high-precision Hugoniot, which is essential to differentiate between the proposed mix models. This study offers EOS data for the 50:50 molar ratio of H_2 -He precompressed to 0.1–0.2 GPa.

V. VALIDATING MIXTURE MODELS

With the experimental and *ab initio* data fully presented, we can now discuss to what extent our different experimental apparatus is capable of testing mixture models. We believe that with current capabilities in the current system, the experiment can distinguish between Amagat ideal mix and a full DFT nonideal mix calculation, albeit with caveats.

To be precise, the ability for experiment to distinguish between mixture models depends in a rigorous statistical sense on three things: (i) the magnitude of the differences between the mixture models (in whichever diagnostic space we choose), (ii) the error bars on the experimental data points, and (iii) the number of experimental data points collected. We will focus on using the Hugoniot in terms of P and ρ as the discriminator between our models, but what we will describe is general for other collections of variables.

We have adopted the following procedure to analyze model discrepancies to rigorously quantify the difference between models and data. Following the most frequent statistical approach, we formulate our null hypothesis as “the experimental data is drawn from the model” or, in common parlance, “the experimental data agrees with the model.” The ensemble of experimental data points is viewed as having been drawn from a multidimensional Gaussian distribution somewhere along the model curve with standard deviations of each variable consistent with the experimentally reported 1σ error bars.

Rigorously speaking, the observed experimental data point could have come from many points along the model curve.

TABLE II. Z -scores for the experimental data relative to DFT (Z_{DFT}) and relative to DFT-Amagat mixing (Z_{AMAGAT}). The italicized numbers represent Z -scores that are sufficient to reject the null hypothesis that “the data is drawn from the model.”

Precompression	Shot ID	Z_{DFT}	Z_{AMAGAT}
$P = 0.11$	STAR40	2.38	<i>6.71</i>
	Z3668S	0.49	0.51
$P = 0.15$	STAR24	1.05	0.77
	STAR20	1.33	1.76
	STAR38	1.78	5.22
	STAR30	0.68	1.74
	STAR39	1.09	0.23
$P = 0.24$	STAR31	2.01	<i>5.17</i>
	Z3492	0.12	0.07
	Z3546S	<i>5.02</i>	2.32
	Z3546N	<i>3.91</i>	2.79

The correct procedure would be to integrate the probabilities over all possible deviations from the model curve, but to simplify this analysis, we define the deviation between the model and an experimental data point as the multidimensional vector from the experimental datum to a point on the model curve that has the highest probability, or lowest Z -score for Gaussian distributions. We consider the DFT and DFT-Amagat curves in Fig. 4 as our two models. We aggregate the experimental data into three bins based on density corresponding to the initial precompression pressures of $P = 0.11$ GPa, $P = 0.15$ GPa, and $P = 0.24$ GPa.

For each bin, we take our DFT and DFT-Amagat curves and, following the procedure in the previous paragraph, compute the maximum probability deviations and Z -scores associated with each experimental datum for each model. We present the results of this in Table II. Taking $Z > 3$ as a cutoff value for rejecting the null hypothesis, based on the individual Z -scores in Table II, we find that for $P = 0.11$ GPa and $P = 0.15$ GPa precompressed Hugoniot, the experimental data favor the DFT model over the Amagat model. In fact, STAR40 rules out the Amagat mix model for $P = 0.11$ GPa, and both STAR38 and STAR31 individually rule out the Amagat mix model for $P = 0.15$ GPa. The situation is reversed for the $P = 0.24$ GPa case, where both Z3546S and Z3546N show sufficiently large Z -scores to reject the DFT null hypothesis, but insufficiently large Z -scores to reject it for the Amagat-DFT mix model.

In Table III, we look at the mean deviations of ρ/ρ_0 and P relative to the DFT and DFT-Amagat mix for all experimental data, for each precompression individually, and in aggregate. Note that we assume normal uncorrelated distributions for the ρ/ρ_0 and P variables, allowing us to use equations for combining uncorrelated error bars on the mean deviation of ρ/ρ_0 and P . Our null hypothesis in this case is that the mean deviations of the experimental data from the model are zero—if the mean deviation was statistically different from zero, this would imply some bias between the experiment and model. This analysis shows roughly equivalent results when considering shot-by-shot Z -scores. We find that both the ρ/ρ_0 and P experimental data are statistically different from the Amagat-DFT model at $P = 0.11$ GPa, and ρ/ρ_0 is

TABLE III. Mean deviations of DFT and DFT-Amagat models relative to all experimental data collected in this work. The first six rows are the mean deviations of ρ/ρ_0 and P for the three considered precompressions. The final row is the mean deviation of ρ/ρ_0 and P for the entire data set. Italicized entries correspond to greater than $3\text{-}\sigma$ deviations.

P_0 (GPa)	Quantity	DFT mean error	Amagat mean error
0.11	ρ/ρ_0	-0.183(95)	-0.514(95)
	P (GPa)	0.82(59)	1.82(59)
0.15	ρ/ρ_0	0.067(57)	-0.386(57)
	P (GPa)	-0.05(17)	0.29(17)
0.24	ρ/ρ_0	0.35(7)	-0.15(7)
	P (GPa)	-8.3(2.5)	5.4(2.5)
Total	ρ/ρ_0	0.123(39)	-0.327(39)
	P (GPa)	-0.02(16)	0.43(16)

statistically different from Amagat-DFT for $P = 0.15$ GPa. At $P = 0.24$ GPa, DFT has a statistically significant deviation from both the ρ/ρ_0 and P experimental data. When combining all the data, we see that for ρ/ρ_0 , DFT has a smaller mean error relative to experiment than the DFT-Amagat mix model. Most importantly, there is a strong, statistically significant difference between these two models. This is true both within a given precompression and in aggregate. While the above analysis yields that neither model can reproduce all the experimental data to $< 3 - \sigma$, we can distinguish between the two and determine that DFT is in better agreement with the experimental data for $P = 0.11$ GPa and $P = 0.15$ GPa and in aggregate than the DFT-Amagat mix model, which does better when considering the $P = 0.24$ GPa data only.

For the lower precompressions, that DFT is a better model is not surprising. DFT-Amagat neglects nonideal mix effects, whereas the full DFT simulation naturally includes these. In Fig. 4, we can see large differences for $P = 0.11$ GPa and $P = 0.15$ GPa precompression Hugoniot between 4 and 30 GPa, which is entirely attributed to the presence of nonideal mixing effects in the DFT. At $P = 0.24$ GPa, it is puzzling that DFT-Amagat is in better agreement with the experiment than DFT since a comparison of the two indicates that nonideal mixing effects should still be present in this regime. Resolving this discrepancy is left for future computational and experimental work.

VI. CONCLUSIONS

To summarize, we have measured the Hugoniot data for precompressed $\text{H}_2\text{-He}$ mixtures in a regime not previously accessed, directly relevant to conditions found in planetary interiors. Our results show a 3- to 4.3-fold density compression at pressures between 8 and 44 GPa, in good agreement with FPMD Hugoniot computed using the PBE functional. Knowing the exact pressure-temperature conditions and physical states of $\text{H}_2\text{-He}$ provides valuable constraints for the chemical components of the layer boundaries, which are crucial in understanding the origin of magnetic fields of the gas giants. The insights and the experimental data obtained from the current study provide a much-needed benchmark for future theoretical

works, such as quantum Monte Carlo calculations and shed light into understanding the interiors of the Jovian-like gas-giant planetary systems.

ACKNOWLEDGMENTS

We thank T. Mattsson for providing valuable feedback on the manuscript; L. Pacheco, K. Hodge, J. Martinez, and C. S. Alexander for their technical assistance;

and the entire Z-team for all the assistance in executing the Z experiments. Sandia National Laboratories is a multimission laboratory managed and operated by National Technology and Engineering Solutions of Sandia, LLC, a wholly owned subsidiary of Honeywell International Inc., for the U.S. Department of Energy's National Nuclear Security Administration under Contract No. DE-NA0003525. This paper describes objective technical results and analysis. Any subjective views or opinions that might be expressed in the paper do not necessarily represent the views of the U.S. Department of Energy or the United States Government.

-
- [1] Z.-G. Li, Q.-F. Chen, Y.-J. Gu, J. Zheng, and X.-R. Chen, Measurements of the principal Hugoniot of dense gaseous deuterium-helium mixtures: Combined multichannel optical pyrometry, velocity interferometry, and streak optical pyrometry measurements, *AIP Adv.* **6**, 105309 (2016).
- [2] G.-J. Li, Z.-G. Li, Q.-F. Chen, Y.-J. Gu, W. Zhang, L. Liu, H.-Y. Geng, Z.-Q. Wang, Y.-S. Lan, Y. Hou, J.-Y. Dai, and X.-R. Chen, Multishock to quasi-isentropic compression of dense gaseous deuterium-helium mixtures up to 120 GPa: Probing the sound velocities relevant to planetary interiors, *Phys. Rev. Lett.* **126**, 075701 (2021).
- [3] M. A. Morales, S. Hamel, K. Caspersen, and E. Schwegler, Hydrogen-helium demixing from first principles: From diamond anvil cells to planetary interiors, *Phys. Rev. B* **87**, 174105 (2013).
- [4] W. Lorenzen, B. Holst, and R. Redmer, Demixing of hydrogen and helium at megabar pressures, *Phys. Rev. Lett.* **102**, 115701 (2009).
- [5] S. Hamel, M. A. Morales, and E. Schwegler, Signature of helium segregation in hydrogen-helium mixtures, *Phys. Rev. B* **84**, 165110 (2011).
- [6] M. Schöttler and R. Redmer, *Ab Initio* calculation of the miscibility diagram for hydrogen-helium mixtures, *Phys. Rev. Lett.* **120**, 115703 (2018).
- [7] F. Soubiran, S. Mazevet, C. Winisdoerffer, and G. Chabrier, Optical signature of hydrogen-helium demixing at extreme density-temperature conditions, *Phys. Rev. B* **87**, 165114 (2013).
- [8] B. Militzer, F. Soubiran, S. M. Wahl, and W. Hubbard, Understanding Jupiter's interior, *JGR Planets* **121**, 1552 (2016).
- [9] G. Chabrier, S. Mazevet, and F. Soubiran, A new equation of state for dense hydrogen-helium mixtures, *Astrophys. J.* **872**, 51 (2019).
- [10] W. J. Nellis, S. T. Weir, and A. C. Mitchell, Minimum metallic conductivity of fluid hydrogen at 140 GPa (1.4 Mbar), *Phys. Rev. B* **59**, 3434 (1999).
- [11] P. Loubeyre, S. Brygoo, J. Eggert, P. M. Celliers, D. K. Spaulding, J. R. Rygg, T. R. Boehly, G. W. Collins, and R. Jeanloz, Extended data set for the equation of state of warm dense hydrogen isotopes, *Phys. Rev. B* **86**, 144115 (2012).
- [12] M. D. Knudson, M. P. Desjarlais, A. Becker, R. W. Lemke, K. R. Cochrane, M. E. Savage, D. E. Bliss, T. R. Mattsson, and R. Redmer, Direct observation of an abrupt insulator-to-metal transition in dense liquid deuterium, *Science* **348**, 1455 (2015).
- [13] M. D. Knudson and M. P. Desjarlais, High-precision shock wave measurements of deuterium: Evaluation of exchange-correlation functionals at the molecular-to-atomic transition, *Phys. Rev. Lett.* **118**, 035501 (2017).
- [14] G.-J. Li, Y.-J. Gu, Y.-S. Lan, Q.-F. Chen, Z.-G. Li, L. Liu, Z.-Q. Wang, Z.-J. Shen, and X.-R. Chen, Compression of gaseous hydrogen into warm dense states up to 95 GPa using multishock compression technique, *Phys. Rev. B* **107**, 014309 (2023).
- [15] J. Eggert, S. Brygoo, P. Loubeyre, R. S. McWilliams, P. M. Celliers, D. G. Hicks, T. R. Boehly, R. Jeanloz, and G. W. Collins, Hugoniot data for helium in the ionization regime, *Phys. Rev. Lett.* **100**, 124503 (2008).
- [16] J. H. Eggert, P. M. Celliers, D. G. Hicks, J. R. Rygg, G. W. Collins, S. Brygoo, P. Loubeyre, R. S. McWilliams, D. Spaulding, R. Jeanloz, and T. R. Boehly, Shock experiments on pre-compressed fluid helium, *AIP Conf. Proc.* **1161**, 26 (2009).
- [17] P. M. Celliers, P. Loubeyre, J. H. Eggert, S. Brygoo, R. S. McWilliams, D. G. Hicks, T. R. Boehly, R. Jeanloz, and G. W. Collins, Insulator-to-conducting transition in dense fluid helium, *Phys. Rev. Lett.* **104**, 184503 (2010).
- [18] C. T. Seagle, W. D. Reinhart, A. J. Lopez, R. J. Hickman, and T. F. Thornhill, High precision Hugoniot measurements on statically pre-compressed fluid helium, *J. Appl. Phys.* **120**, 125902 (2016).
- [19] S. Brygoo, M. Millot, P. Loubeyre, A. E. Lazicki, S. Hamel, T. Qi, P. M. Celliers, F. Coppari, J. H. Eggert, D. E. Fratanduono, D. G. Hicks, J. R. Rygg, R. F. Smith, D. C. Swift, G. W. Collins, and R. Jeanloz, Analysis of laser shock experiments on pre-compressed samples using a quartz reference and application to warm dense hydrogen and helium, *J. Appl. Phys.* **118**, 195901 (2015).
- [20] Y. J. Gu, Q. F. Chen, L. C. Cai, Z. Y. Chen, J. Zheng, and F. Q. Jing, Multishock comparison of dense gaseous H₂+He mixtures up to 30 GPa, *J. Chem. Phys.* **130**, 184506 (2009).
- [21] Z.-G. Li, Q.-F. Chen, Y.-J. Gu, J. Zheng, W. Zhang, L. Liu, G.-J. Li, Z.-Q. Wang, and J.-Y. Dai, Multishock compression of dense cryogenic hydrogen-helium mixtures up to 60 GPa: Validating the equation of state calculated from first principles, *Phys. Rev. B* **98**, 064101 (2018).
- [22] S. Brygoo, P. Loubeyre, M. Millot, J. R. Rygg, P. M. Celliers, J. H. Eggert, R. Jeanloz, and G. W. Collins, Evidence of hydrogen-helium immiscibility at jupiter-interior conditions, *Nature (London)* **593**, 517 (2021).

- [23] Royal Society of Chemistry, Periodic table, <https://www.rsc.org/periodic-table/element/1/hydrogen> (unpublished).
- [24] Royal Society of Chemistry, Periodic table, <https://www.rsc.org/periodic-table/element/2/helium> (unpublished).
- [25] J. Lim and C. S. Yoo, Phase diagram of dense H₂-H_e mixtures: Evidence for strong chemical association, miscibility, and structural change, *Phys. Rev. Lett.* **120**, 165301 (2018).
- [26] J. Lim, M. Kim, S. Duwal, S. Kawaguchi, Y. Ohishi, H.-P. Liermann, R. Hrubiak, J. S. Tse, and C.-S. Yoo, Compression behavior of dense H₂-He mixtures up to 160 GPa, *Phys. Rev. B* **101**, 224103 (2020).
- [27] See Supplemental Material at <http://link.aps.org/supplemental/10.1103/PhysRevB.109.104102> for more details on the experimental and computational methods and analysis.
- [28] H. K. Mao, P. M. Bell, J. W. Shaner, and D. J. Steinberg, Specific volume measurements of Cu, Mo, Pd, and Ag and calibration of the ruby R₁ fluorescence pressure gauge from 0.06 to 1 Mbar, *J. Appl. Phys.* **49**, 3276 (1978).
- [29] K. R. Cochrane, P. Kalita, J. L. Brown, C. A. McCoy, J. W. Gluth, H. L. Hanshaw, E. Scoglietti, M. D. Knudson, S. P. Rudin, and S. D. Crockett, Platinum equation of state to greater than two terapascals: Experimental data and analytical models, *Phys. Rev. B* **105**, 224109 (2022).
- [30] C. M. Zoller, M. Ahart, S. Duwal, R. C. Clay, C. T. Seagle, Y. J. Ryu, S. Tkachev, S. Chariton, V. Prakapenka, and R. J. Hemley, Accurate equation of state of H₂-He binary mixtures up to 5.4 GPa, *Phys. Rev. B* **108**, 224112 (2023).
- [31] M. D. Knudson and M. P. Desjarlais, Adiabatic release measurements in α -quartz between 300 and 1200 GPa: Characterization of α -quartz as a shock standard in the multimegabar regime, *Phys. Rev. B* **88**, 184107 (2013).
- [32] M. P. Desjarlais, M. D. Knudson, and K. R. Cochrane, Extension of the Hugoniot and analytical release model of α -quartz to 0.2–3 TPa, *J. Appl. Phys.* **122**, 035903 (2017).
- [33] R. Le Toullec, P. Loubeyre, and J.-P. Pinceaux, Refractive-index measurements of dense helium up to 16 GPa at $T = 298$ K: Analysis of its thermodynamic and electronic properties, *Phys. Rev. B* **40**, 2368 (1989).
- [34] H. Shimizu, E. M. Brody, H. K. Mao, and P. M. Bell, Brillouin measurements of solid n -H₂ and n -D₂ to 200 kbar at room temperature, *Phys. Rev. Lett.* **47**, 128 (1981).
- [35] A. Polian and M. Grimsditch, Elastic properties and density of helium up to 20 GPa, *Europhys. Lett.* **2**, 849 (1986).
- [36] A. Dewaele, J. H. Eggert, P. Loubeyre, and R. Le Toullec, Measurement of refractive index and equation of state in dense He, H₂, H₂O, and Ne under high pressure in a diamond anvil cell, *Phys. Rev. B* **67**, 094112 (2003).
- [37] P. Hohenberg and W. Kohn, Inhomogeneous electron gas, *Phys. Rev.* **136**, B864 (1964).
- [38] W. Kohn and L. J. Sham, Self-consistent equations including exchange and correlation effects, *Phys. Rev.* **140**, A1133 (1965).
- [39] R. J. Magyar and T. R. Mattsson, Mixing of equations of state for xenon-deuterium using density functional theory, *Phys. Plasmas* **20**, 032701 (2013).
- [40] G. Kresse and J. Hafner, *Ab initio* molecular dynamics for liquid metals, *Phys. Rev. B* **47**, 558 (1993).
- [41] G. Kresse and J. Furthmüller, Efficient iterative schemes for *ab initio* total-energy calculations using a plane-wave basis set, *Phys. Rev. B* **54**, 11169 (1996).
- [42] N. D. Mermin, Thermal properties of the inhomogeneous electron gas, *Phys. Rev.* **137**, A1441 (1965).
- [43] J. P. Perdew, K. Burke, and M. Ernzerhof, Generalized gradient approximation made simple, *Phys. Rev. Lett.* **77**, 3865 (1996).
- [44] M.-A. Schaeuble, T. Nagayama, J. E. Bailey, B. H. Dunlap, and S. Patel, Experimental methods for laboratory measurements of helium spectral line broadening in white dwarf photospheres, *Phys. Plasmas* **28**, 062902 (2021).